CHEMISTRY OF MATERIALS

pubs.acs.org/cm

Article

Colloidal Synthesis of Homogeneous $Ge_{1-x-y}Si_ySn_x$ Nanoalloys with Composition-Tunable Visible to Near-IR Optical Properties

Drew Spera, David Pate, Griffin C. Spence, Corentin Villot, Chineme Jeanfrances Onukwughara, Daulton White, Ka Un Lao, Ümit Özgür, and Indika U. Arachchige*

Cite This: *Chem. Mater.* 2023, 35, 9007−9018

Read Online

ACCESS | Metrics & More | Article Recommendations | Supporting Information

ABSTRACT: Group IV alloy nanocrystals (NCs) are a class of direct energy gap semiconductors that show high elemental abundance, low to nontoxicity, and composition-tunable absorption and emission properties. These properties have distinguished $Ge_{1-x}Sn_x$ NCs as intriguing materials for near-infrared (IR) optical studies. Achieving a material with efficient visible emission requires a modified class of group IV alloys, and the computational studies suggest that this can be achieved with $Ge_{1-x-y}Si_ySn_x$ NCs. Herein, we report a colloidal strategy for the synthesis of bulk-like (10.3 ± 2.5−25.5 ± 5.3 nm) and quantum-confined (3.2 ± 0.6−4.2 ± 1.1 nm) $Ge_{1-x-y}Si_ySn_x$ alloys that show strong size confinement effects and composition-tunable visible to near IR absorption and emission properties. This synthesis produces a homogeneous alloy with a diamond cubic Ge structure and tunable Si (0.9−16.1%) and Sn (1.8−14.9%) compositions, exceeding the equilibrium solubility of Sn (<1%) in crystalline Si and Ge. Raman spectra of $Ge_{1-x-y}Si_ySn_x$ alloys show a prominent red-shift of the Ge−Ge peak and the emergence of a Ge−Si peak with increasing Si/Sn, suggesting the growth of homogeneous alloys. The smaller $Ge_{1-x-y}Si_ySn_x$ NCs exhibit absorption onsets from 1.21 to 1.94 eV for x = 1.8−6.8% and y = 0.9−16.1% compositions, which are blue-shifted from those reported for $Ge_{1-x-y}Si_ySn_x$ bulk alloy films and $Ge_{1-x}Sn_x$ alloy NCs, indicating the influence of Si incorporation and strong size confinement effects. Solid-state photoluminescence (PL) spectra reveal core-related PL maxima from 1.77−1.97 eV in agreement with absorption onsets, consistent with the energy gaps calculated for ∼3−4 nm alloy NCs. With a facile, low-temperature solution synthesis and direct control over physical properties, this methodology presents a noteworthy advancement in the synthesis of bulk-like and quantum-confined $Ge_{1-x-y}Si_ySn_x$ alloys as versatile materials for future optical and electronic studies.

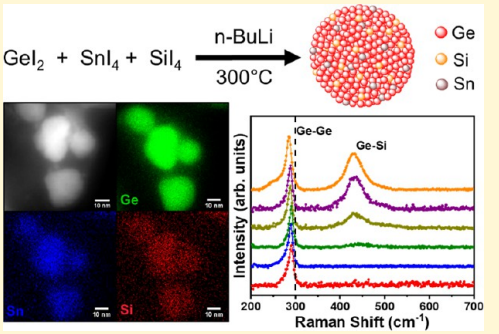

INTRODUCTION

Semiconductor nanocrystals (NCs) are a fascinating class of materials that show unique size and shape-tunable optical properties, making them attractive for solar photovoltaics,[1,2] photocatalysis,[3−5] sensing,[6] imaging,[7,8] and light-emitting[9] technologies. Of particular interest are the nanostructures produced from group IV elements, Si, Ge, and their Sn-containing alloys. These materials exhibit several advantages over other semiconductor (CdSe, PbS, HgS, and $CsPbCl_3$, etc.) systems including low to nontoxicity,[10] high elemental abundancy,[11] and compatibility with complementary metal−oxide−semiconductor (CMOS) technology. The optical properties of group IV alloys can be tuned by varying the size and/or composition.[12−14] This results in a wider range of energy gaps and, consequently, absorption and emission properties that can be tuned by altering the synthesis parameters. Additionally, group IV alloy NCs display a key advantage over the corresponding bulk counterparts, owing to their quantum confinement-modified electronic structure. Bulk Si and Ge are limited in applicability because of their fundamental indirect band structure, which drastically decreases the absorption and emission efficiency.[15] However, for smaller quantum-confined NCs, the electronic structure ceases to resemble a continuous network of possible states and begins to approximate a more familiar HOMO−LUMO structure.[16] This eliminates the disadvantages of indirect energy gaps and improves the optical efficiency.

Theoretical and experimental studies have shown that bulk Si and Ge can experience an indirect to direct−gap transition at sufficiently high levels of Sn alloying.[17] This transition stems from the expansion of Si or Ge structure by α-Sn, the diamond-like structural equivalent to Si and Ge; however, a few problems limited the application of this effect in optical devices. Because Sn is a conductor (band gap = 0.08 eV), the incorporation of Sn reduces the energy gaps and promotes a

Received: June 30, 2023
Revised: September 28, 2023
Published: October 16, 2023

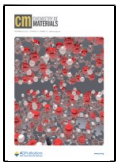

Scheme 1. Scheme Illustrating the Synthetic Procedure for Quantum-Confined and Nonquantum Confined $Ge_{1-x-y}Si_ySn_x$ Alloy NCs, where the Time Held at 300 °C is a Determining Factor for Synthesis of Larger NCs (15 min) and Smaller QDs (5 min)

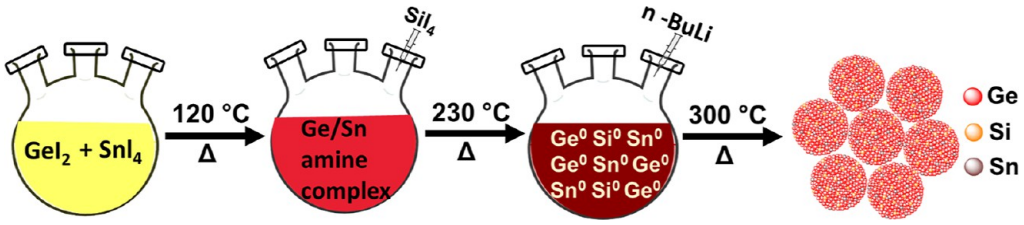

metallic character of bulk alloys, eliminating any potential in visible to near IR optical studies. Moreover, the bulk solubility of Sn in Si and Ge is notoriously low (<1%) because of the larger differences in lattice constants; thus, the first GeSiSn alloys with sufficient Sn to produce direct-gaps were fabricated as thin films via careful strain engineering.[18] This has been accomplished through low-temperature nonequilibrium growth processes, such as molecular beam epitaxy (MBE)[19] and chemical vapor deposition (CVD).[20] MBE studies report homogeneous GeSiSn films with 3−15 and 12−58% Si and Sn compositions, respectively.[21,22] CVD methods, which are more popular than MBE, report 1.8−5.8% and 3.2−10% Si and Sn contents, respectively, and a transition to a direct band structure when the Sn content is greater than Si.[23−25] These films show significant (5×) photoluminescence enhancement with increasing the Sn content from 5.1 to 8.3%, caused by the increased lattice disorder.[25] However, these traditional vapor phase synthetic methods often admit to stacking faults, crystal imperfections, and Sn segregation for samples with a Sn content greater than ∼15−20%.[26,27]

The structurally homogeneous $Ge_{1-x}Sn_x$ alloy NCs and quantum dots (QDs), on the other hand, have been recently synthesized via wet chemical methods with Sn content up to 95%,[28] eliminating the Sn segregation entirely. This has been generally attributed to low-temperature growth and unique strain relaxation that allow smaller NCs to reduce the stress from lattice inhomogeneity, making a wider range of alloy compositions stable.[29] Our group has reported the solution synthesis and optical and electrical characterization of 1.8−2.2,[13,14,30] 3−5,[12] 5−7,[31] and 15−23 nm[12] of $Ge_{1-x}Sn_x$ alloys and their solution-processed thin films,[32] with Sn content up to ∼28%. The confinement energy inherent to $Ge_{1-x}Sn_x$ QDs results in wider direct energy gaps primarily in the near IR spectrum.[14,31] The admixture of Sn increases the oscillator strengths of optical transitions,[30] further improving the optical efficiency of alloy QDs. Although a few theoretical studies on GeSiSn alloys and QDs are reported,[33,34] the synthesis of ternary GeSiSn alloys as discrete nanostructures and their optical property investigation as a function of morphology, composition, and confinement effects has not been reported.

Herein, we report a facile low-temperature colloidal synthetic strategy for $Ge_{1-x-y}Si_ySn_x$ alloys via coreduction of halide precursors in alkylamine and alkane surfactant/solvent mixtures. Synthetic parameters were carefully tuned to produce bulk-like (10.3 ± 2.5−25.5 ± 5.3 nm) and quantum-confined (3.2 ± 0.6−4.2 ± 1.1 nm) ternary alloys with variable Si (0.9−16.1%) and Sn (1.8−14.9%) compositions. As-synthesized alloys retain the diamond cubic structure of Ge with a shift of diffraction patterns to lower 2θ angles with increasing Sn compositions. This, along with red-shifting of Ge−Ge phonon mode and appearance of a Ge−Si phonon mode, and elemental maps confirm the structural homogeneity of solution-synthesized $Ge_{1-x-y}Si_ySn_x$ alloys. The smaller QDs exhibit composition-tunable absorption onsets and emission maxima from 1.21−1.94 and 1.77−1.97 eV for x = 1.8−6.8% and y = 0.9−16.1% compositions, respectively. These transition energies are significantly higher than those reported for GeSiSn thin films and ∼3−5 nm $Ge_{1-x}Sn_x$ alloy QDs,[35] signifying the effects of Si incorporation and strong size confinement effects. This constitutes an expansion of the optical properties that can be achieved for group IV alloy NCs.

EXPERIMENTAL SECTION

Materials. Germanium(II) iodide (GeI_2, 99.999%) was purchased from Strem Chemicals. Tin(IV) tetraiodide (SnI_4, 99.99%) and silicon(IV) iodide (SiI_4, 99%) were purchased from Alfa Aesar. Oleylamine (OLA, 98%), 1-octadecene (ODE, 90%), and *n*-butyllithium (*n*-BuLi, 1.6 M in hexane) were purchased from Sigma-Aldrich. ACS grade toluene and methanol were purchased from Fisher before being distilled over nitrogen and stored over molecular sieves. OLA and ODE were dried under vacuum at 120 °C for 90 min prior to use. All other chemicals were used as received. *[Important: Butyl-lithium compounds are extremely pyrophoric and should be handled by properly trained personnel under strict air-free conditions.]*

Preparation of SiI_4 Stock Solution. The SiI_4 stock solution was prepared by mixing 0.2679 g of SiI_4 into 10 mL of an OLA under N_2 in a glovebox. Afterward, this mixture was taken out of the glovebox and connected to a Schlenk line, where it was heated under vacuum at 120 °C for 60 min. Then, the flask was cooled to ∼60 °C while still under vacuum before it was transferred to the glovebox and emptied into a 20 mL glass vial for storage.

Synthesis of ∼10−25 nm $Ge_{1-x-y}Si_ySn_x$ Alloy NCs. In a glovebox under a N_2 atmosphere, an appropriate amount of GeI_2 and SnI_4 (Supporting Information, Table S1) were dispersed in 10 mL OLA in a three-necked flask with a condenser, septum, and thermocouple. Separately, a solution of 1.1 mL of *n*-BuLi dispersed in 3.0 mL of ODE was prepared under a nitrogen atmosphere. An appropriate volume of SiI_4/OLA stock solution was drawn into a disposable syringe. The flask, *n*-BuLi solution, and SiI_4 syringe were all removed from the glovebox, and the flask was connected to a Schlenk line where it was degassed and flushed with nitrogen three times (Scheme 1).

Next, while under a vacuum, the temperature of the flask was increased to 120 °C under high stirring, where it was held for 25 min. At this stage, the solution takes on a red-orange color as the Ge and Sn precursors complex with the OLA. After 25 min, the solution was placed under nitrogen and the temperature was increased to 230 °C. At 230 °C, the SiI_4/OLA solution was swiftly injected. Then, the temperature was decreased to 210 °C, where the reaction was allowed to spin for an additional 20 min. The temperature was then increased to 230 °C, at which point the *n*-BuLi solution was injected. Finally, the temperature was raised to 300 °C, where the reaction was held for 15 min before quenching by removal from the heating mantle and cooling with compressed air.

https://doi.org/10.1021/acs.chemmater.3c01644
Chem. Mater. 2023, 35, 9007−9018

After the reaction, the flask was emptied in a 50 mL centrifuge tube. Then, ∼20 mL of methanol was added to precipitate the $Ge_{1-x-y}Si_ySn_x$ alloy NCs. The reaction was centrifuged for 10 min, after which the clear supernatant was discarded, and the pellet was dissolved in ∼5 mL of toluene. After a 5 min centrifuge, the pellet, containing any aggregates or impurities, was discarded, and the supernatant was transferred to another centrifuge tube and again precipitated with ∼20 mL methanol. This procedure was repeated three times to create a thoroughly washed product. For solid-state analysis, the pellet after precipitation via methanol was used, whereas, for transmission electron microscopy (TEM) analysis, a small amount of this product was dispersed in toluene and deposited onto a TEM grid.

Synthesis of 3.2−4.2 nm $Ge_{1-x-y}Si_ySn_x$ Alloy QDs. The synthetic method for smaller $Ge_{1-x-y}Si_ySn_x$ QDs is similar to that of the larger NCs, but with several key differences. First, an appropriate amount of GeI_2 and SnI_4 precursors (Supporting Information, Table S2) and 20 mL of OLA were placed in a 50 mL round-bottom flask outfitted with a septa and thermocouple. Then, 1.1 mL of *n*-BuLi was separately dispersed in 3.0 mL of ODE in a 20 mL glass vial. A proportional amount of the SiI_4 stock solution was drawn into a syringe. The flask was then removed from the glovebox and placed under vacuum, where it was heated to 120 °C and kept under high stirring for 25 min. Next, the flask was purged with nitrogen, and the temperature was increased to 230 °C for the injection of the SiI_4 precursor. The temperature then decreased to ∼210 °C, where it was kept under stirring for an additional 20 min. Then, the temperature was increased to 230 °C again, and the *n*-BuLi/ODE solution was injected. This produced a mild smoke, and the reaction turned to dark brown/black color. Finally, the temperature was raised to 300 °C, and the reaction was held for 5 min before being quenched with compressed air.

After synthesis, the solution was emptied into a 50 mL centrifuge tube, which was filled with ∼20 mL of methanol. This precipitated the product QDs after centrifugation at 6000 rpm for 10 min. The supernatant was discarded before redispersing the pellet in 5 mL of toluene and centrifuging for 5 min, after which the supernatant was transferred to a new centrifuge tube and the pellet was discarded. Next, a size-selective precipitation method was used to eliminate bulk-like particles and narrow the size dispersity.[36,37] To the NC solution in toluene were added 60 drops of methanol via a transfer pipet. The resulting solution was centrifuged for 10 min at 6000 rpm, the pellet, referred to as the first fraction, was discarded. Then, 20 drops of methanol were added, followed by another 10 min centrifugation. This time, the pellet was kept and used for analysis. This fraction contained the narrowly dispersed quantum-confined particles of interest. The remaining supernatant, containing mostly small clusters, was discarded.

Physical Characterization. A Cary 6000i UV−Vis−near IR spectrophotometer (Agilent Technologies) was used in the double beam mode to record solution state UV−Vis−NIR absorption spectra of all samples. Solid-state diffuse reflectance spectra were recorded using an internal diffuse reflectance DRA 2500 attachment with a $BaSO_4$ background holder. The Kubelka−Munk remission function was used to convert the measured reflectance to absorption.[38,39] Powder diffraction patterns were recorded using Malvern PANalytical PXRD equipped with Cu Kα (λ = 1.5418 Å) radiation. This instrument is regularly calibrated using a Si standard with a diameter of 32 mm and a thickness of 2 mm. The Scherrer formula was used to calculate the crystallite size. Raman spectra were recorded by using a Thermo Scientific DXR Raman spectrophotometer equipped with a 532 nm laser. An energy-dispersive spectroscopy (EDS) unit attached to scanning electron microscopy (SEM) operating at 15 keV was used to investigate the composition. The samples were attached using double-sided carbon tape, and the composition of each sample was determined by averaging the atomic percentages of five individual spots per sample. TEM images, scanning transmission electron microscopy (STEM), and high-angle annular dark field images (HAADF) were recorded with a JEM-F200 Cold FEG electron microscope operating at 200 kV. Samples were prepared by dispersing a small amount of NCs in toluene before drop-casting onto carbon-coated copper grids. Lattice spacings of alloy NCs were calculated by plotting the inverse FFT images of particles acquired via ImageJ and dividing the distance by a set number of peaks (15−30). This procedure was repeated with multiple NCs to confirm a consistent spacing. Room-temperature photoluminescence (PL) spectra of the drop-cast samples were measured by utilizing Kimmon 325 nm HeCd and Coherent Obis 405 nm lasers in conjunction with a liquid nitrogen-cooled CCD detector mounted onto a 30 cm focal length spectrograph. For PL measurements under vacuum, the samples were mounted within a Janis cryostat evacuated to a pressure of $\sim 10^{-4}$ Torr, with excitation/collection through an integrated quartz window. Peak positions were extracted from multi-Gaussian fits to measured PL spectra.

Computational Energy Gap Calculations. $Ge_{1-x-y}Si_ySn_x$ QDs were constructed by first generating pure Ge QDs of various sizes with coordinates set to the lattice constant of bulk Ge (5.66 Å). The composition of QDs was modified by homogeneously substituting Ge atoms with Si and Sn atoms, whereas the surface was passivated with hydrogen atoms. For each QD size/composition combination, the geometries of the ground state were optimized by using the local spin-density approximation at the level of SPW92/def2-SVP with the corresponding effective core potentials on Sn. The def2-SVP basis set, however, became intractable for QDs with large diameters; thus, the HWMB basis set was used for larger QDs. The SPW92/HWMB approach overestimated the lattice constant, which subsequently caused a bias in the energy gap calculations. To correct this bias, the energy gaps were computed at the level of HLE16/CRENBL using 1.407, 1.715, and 2.131 nm QDs optimized using both SPW92/def2-SVP and SPW92/HWMB and each set was fitted with a power law curve. The mean bias between the two curves in the interpolation area was obtained, used as a correction factor, and added to the HLE16/CRENBL//SPW92/HWMB energy gap values. After a bias correction, the number of HLE16/CRENBL//SPW92/HWMB gaps needed was determined based on the accuracy of the extrapolation curve to bulk Ge. This approach was used for subsequent extrapolation of energy gaps, using five QD sizes in the range of ∼1.4 to 3 nm. All calculations were performed using a locally modified version of Q-Chem.[40]

RESULTS AND DISCUSSION

Synthesis of Bulk-Like $Ge_{1-x-y}Si_ySn_x$ Alloy NCs. To date, there are no reports on the colloidal or wet chemical synthesis of $Ge_{1-x-y}Si_ySn_x$ alloys.[12,29] A colloidal strategy allows for synthesis of bulk-like and quantum-confined alloys, allowing for investigation of size- and composition-dependent optical properties, which are not possible with traditional vapor phase syntheses. However, there were major challenges with designing an effective low-temperature solution synthesis for $Ge_{1-x-y}Si_ySn_x$ alloys. For instance, Si is very sensitive to oxidation, especially in comparison to Ge and Sn. This not only gives the Schenk line and oxygen free methodology an additional importance but also necessitates the use of relatively inert solvents, especially those creating a reductive environment (i.e., amines), whereas use of oleic acid or some other carboxylates can result in the Si-oxidation to SiO_2, preventing the growth of homogeneous alloys. Moreover, careful diligence is essential with the preparation of the SiI_4 stock, which was kept under rigorous air and moisture free conditions when handling under an ambient atmosphere. This is also because contamination from oxygen causes Si to oxidize, precipitate, and become unusable.

In this study, halide precursors dispersed in an OLA solvent were reduced by *n*-BuLi into atomic monomers, which crystallize to produce nanoalloys. Ge and Sn halides are added in the solid state, whereas the Si precursor is freshly prepared by dissolving SiI_4 in the OLA and mixed with the Ge/

https://doi.org/10.1021/acs.chemmater.3c01644
Chem. Mater. 2023, 35, 9007−9018

Sn precursors at a later stage. This latter addition helps minimize unfavorable side reactions and avoids the formation of Si^0 or SiO_x byproducts. It was found that the SiI_4 stock solution is stable for ∼7 days before there is a significant chance of precipitation. To avoid β-Sn impurities, the temperature must be maintained below 230 °C prior to *n*-BuLi reduction. Sn has a melting point of ∼231.9 °C, and any Sn^0 atoms present at this temperature can produce thermodynamically more stable β-Sn impurities. Lastly, the temperature is increased to 300 °C where the alloy nuclei were grown for 5 min (smaller QDs) or 15 min (larger NCs) prior to reaction being quenched and NCs were purified and isolated. Initially, a set of larger (10.3 ± 2.5−25.5 ± 5.3 nm) nonquantum-confined alloys were produced to adequately study the changes in structural characteristics. Subsequent efforts were shifted to produce smaller (3.2 ± 0.6−4.2 ± 1.1 nm) alloy QDs to probe both the effects of quantum confinement and Si/Sn alloying on optical properties.

Size and morphology of the larger $Ge_{1-x-y}Si_ySn_x$ alloy NCs were investigated via TEM (Figure 1). The average diameters and lattice spacing of particles were calculated using low-resolution TEM images, which are listed in Supporting Information, Table S3. Although the average diameters of the first three compositions (Figure 1A−C) are within ∼6 nm of each other, there is a substantial size increase for the highest alloy composition ($Ge_{0.738}Si_{0.112}Sn_{0.149}$). As studies on GeSn materials have identified, Sn promotes the crystallization and growth of group IV alloys; thus, the increased Sn composition of this sample likely caused the growth of larger polygonal NCs. This could also explain why alloys with a higher Sn content adopt a more angular or polygonal morphology, as opposed to the quasi-spherical nature of alloys having a lower Sn content (Figure 1). The images shown in Figure 1E−H display magnified representative images of individual NCs, where the dominant diamond cubic (111) plane is visible in several NCs. The corresponding fast Fourier transform (FFT) images show polycrystallinity of particles, consisting of multiple crystal domains (Figure S1). The lattice spacings of alloys are closer to that of pure Ge (3.3 Å)[41] and show a minor variation depending on the composition, with the largest being the Sn-rich particles, as shown in Figure 1H with a spacing of ∼3.4 Å.

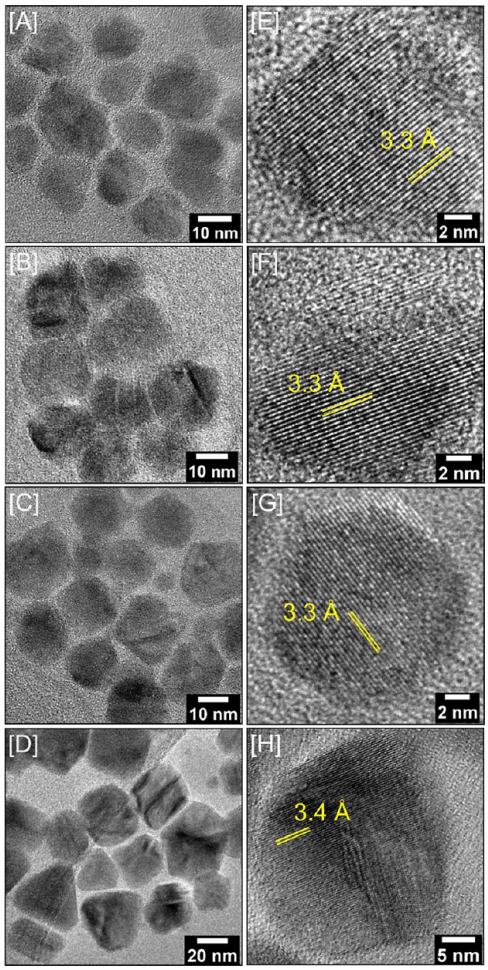

Figure 1. Representative low-resolution and high-resolution TEM images of larger, bulk-like [A,E] $Ge_{0.921}Si_{0.033}Sn_{0.046}$, [B,F] $Ge_{0.842}Si_{0.072}Sn_{0.085}$, [C,G] $Ge_{0.797}Si_{0.121}Sn_{0.083}$, and [D,H] $Ge_{0.738}Si_{0.112}Sn_{0.149}$ alloy NCs with a (111) diamond cubic lattice plane outlined in yellow.

STEM images and elemental maps of the larger alloy NCs are shown in Figures 2 and 3. Each composition reported herein displays an even distribution of Ge, Si, and Sn throughout the diamond cubic lattice, indicative of a homogeneous solid solution. Although Si is notoriously difficult to resolve via elemental mapping, we have used long exposure times on thoroughly purified samples to maximize the signal: noise ratio and optimize the visibility of Si. There is no local segregation of Si or Sn on the surface or core of the NCs, distinguishing these particles as phase pure without any phase segregated impurities and core−shell heterostructures. Additional elemental maps and EDS spectra, as shown in Supporting Information, Figures S2 and S3, respectively, indicate the homogeneous alloying of Ge, Si, and Sn throughout the particles for variable Si (3.34−12.07%) and Sn (4.60−14.96%) compositions. The combined results from TEM, STEM, and elemental maps suggest that these particles are crystalline, colloidally stable, and homogeneous $Ge_{1-x-y}Si_ySn_x$ alloys.

A detailed look at the structural characteristics of larger alloys is presented in Figure 4. PXRD was used to confirm the crystal structure and corroborate the absence of impurities. All compositions studied feature three peaks, indexed to the (111), (220), and (311) planes of a diamond cubic structure, similar to that of Ge (JCPDS # 01-89-5011). Additionally, these reflections are slightly shifted to lower 2θ angles relative to the Ge reference pattern, an effect which has also been identified in GeSn alloys,[12−14,28,29] caused by lattice expansion from Sn incorporation. The principal peak positions of the first three compositions (a−c, Supporting Information, Table S3) are lower than that of the Ge reference pattern, indicating that Sn affects the lattice structure more than Si. The admixture of Sn leads to the expansion of Ge host, whereas the admixture of Si leads to contraction, compensating the effect of Sn addition. Thus, a minimum shift is observed for a−c compositions, signifying a negligible expansion of the Ge host. This is not a surprise because lattice constant for α-Sn (6.489 Å) deviates from Ge (5.646 Å) far more than that of Si (5.431 Å).[42,43] Consequently, the PXRD pattern of $Ge_{0.738}Si_{0.112}Sn_{0.149}$ NCs is shifted to the lowest 2θ values because of the noticeably high Sn content.[44] Importantly, there are no peaks corresponding to the impurities that can be attributed to GeO_2 or β-Sn, commonly found in colloidally synthesized group IV NCs. There is some minor peak broadening in these patterns;

https://doi.org/10.1021/acs.chemmater.3c01644
Chem. Mater. 2023, 35, 9007−9018

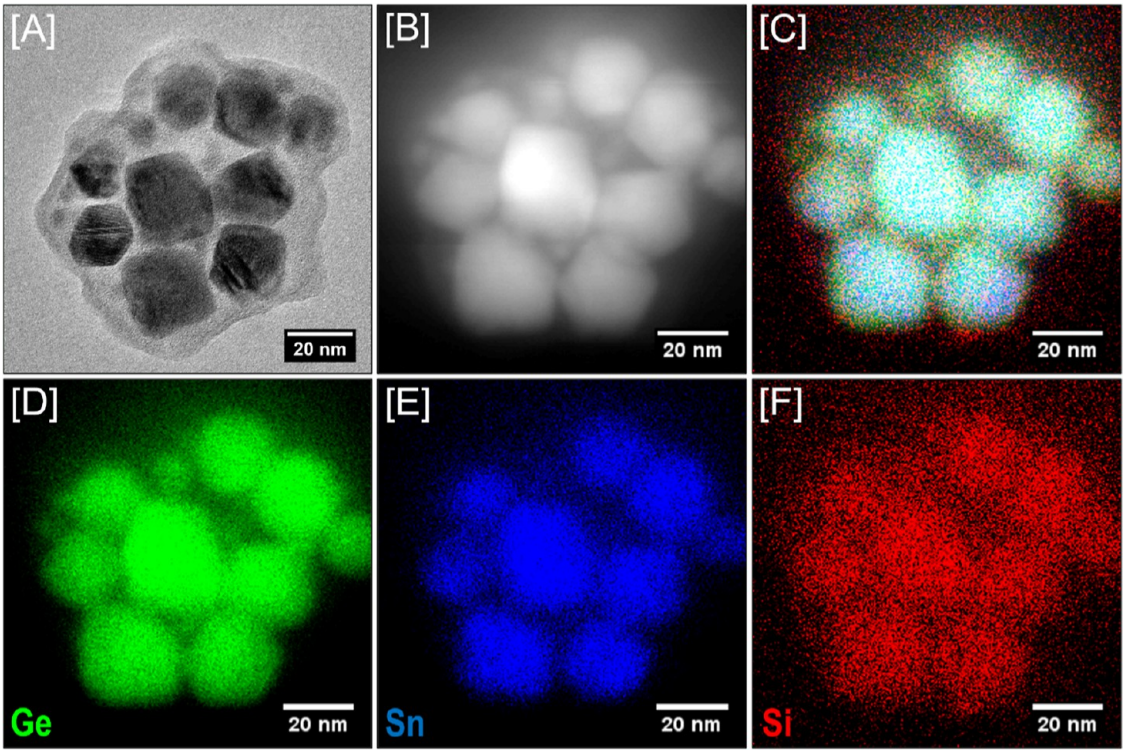

Figure 2. [A] Bright-field and [B] dark-field STEM images and STEM-HAADF elemental maps of [D] Ge, [E] Sn, and [F] Si and [C] an overlay of all elements for $Ge_{0.797}Si_{0.121}Sn_{0.083}$ NCs, demonstrating the structural homogeneity of as-synthesized alloys.

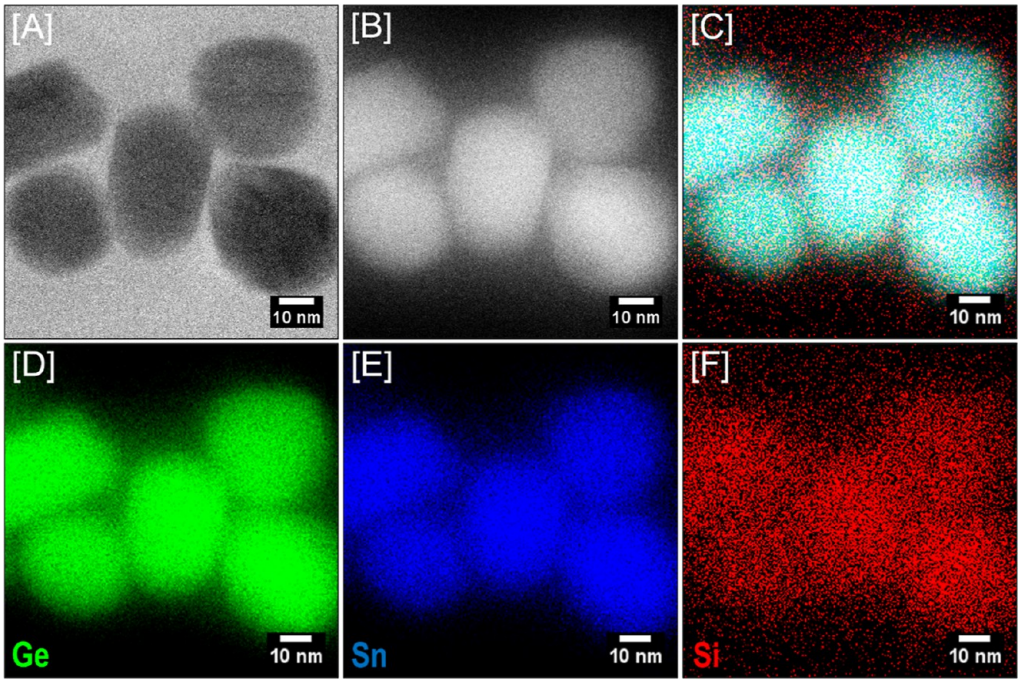

Figure 3. [A] Bright-field and [B] dark-field STEM images of alloy NCs having higher Si and Sn compositions ($Ge_{0.738}Si_{0.112}Sn_{0.149}$) along with STEM-HAADF elemental maps of [D] Ge, [E] Sn, [F] Si, and [C] an overlay of all elements showing the structural homogeneity throughout the alloys.

however, it is not nearly prominent as in our studies on smaller $Ge_{1-x-y}Si_ySn_x$ QDs.

The phonon vibrational modes of alloy NCs were probed via Raman spectroscopy and are shown in Figure 4B. Two peaks attributed to the phonon modes of Ge−Ge and Ge−Si bonds were present in all samples. Bulk Ge exhibits a Raman peak at 300 cm^{-1},[45] whereas single element Ge NCs show a peak at 293 cm^{-1},[46] slightly red-shifted from the bulk Ge. In contrast, the Ge−Ge peaks of the $Ge_{1-x-y}Si_ySn_x$ NCs appear at 283.4−288.8 cm^{-1}, due to the combined effects of alloying and phonon confinement. The large Sn atoms create a Sn−Ge bond, which is longer and weaker than Ge−Ge bonds;

https://doi.org/10.1021/acs.chemmater.3c01644
Chem. Mater. 2023, 35, 9007−9018

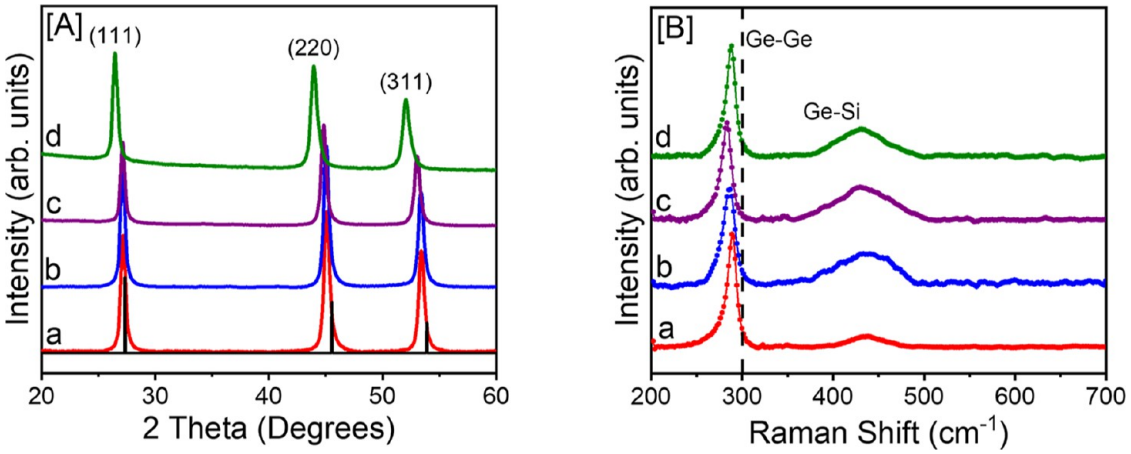

Figure 4. [A] PXRD patterns and [B] Raman spectra of larger (a) $Ge_{0.921}Si_{0.033}Sn_{0.046}$, (b) $Ge_{0.842}Si_{0.072}Sn_{0.085}$, (c) $Ge_{0.797}Si_{0.121}Sn_{0.083}$, and (d) $Ge_{0.738}Si_{0.112}Sn_{0.149}$ alloy NCs. The ICCD-PDF overlay of diamond cubic Ge (JCPDS 01-89-5011) is shown as a vertical black line in [A]. The dotted line in [B] represents the bulk Ge−Ge vibration, which appears at 300 cm^{-1}.

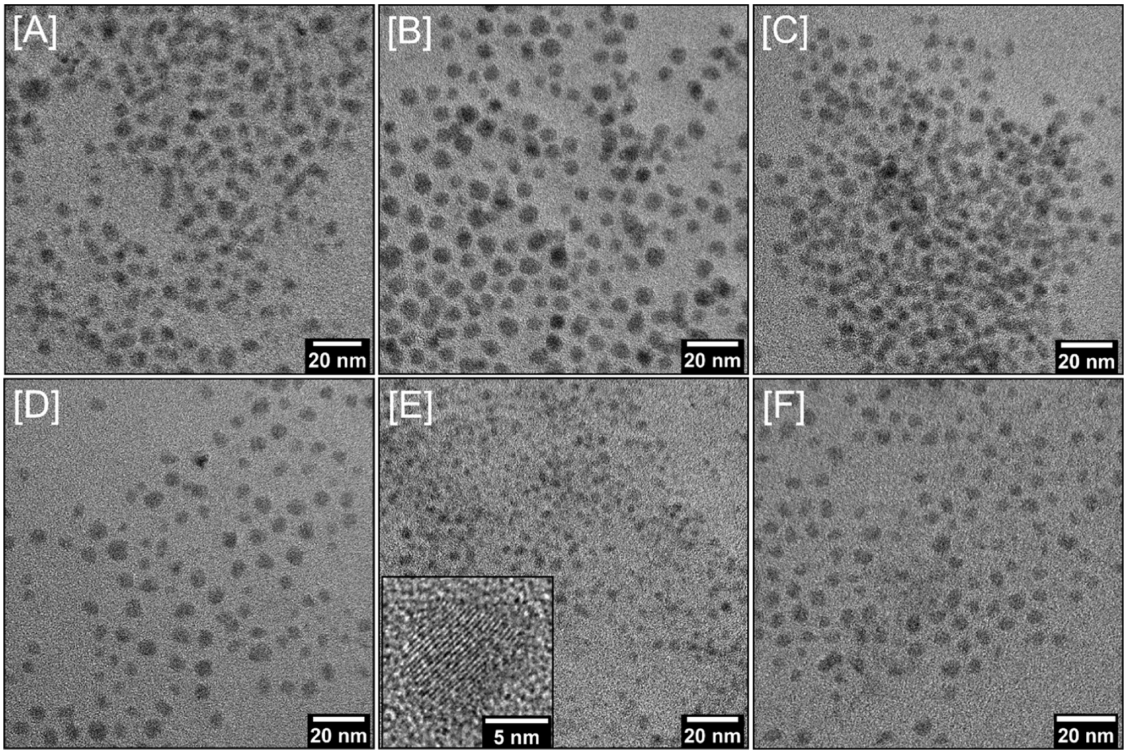

Figure 5. Low-resolution bright field TEM images of quantum confined $Ge_{1-y-x}Si_ySn_x$ alloy NCs with compositions of [A] $Ge_{0.935}Si_{0.009}Sn_{0.056}$, [B] $Ge_{0.945}Si_{0.021}Sn_{0.034}$, [C] $Ge_{0.899}Si_{0.033}Sn_{0.068}$, [D] $Ge_{0.907}Si_{0.075}Sn_{0.018}$, [E] $Ge_{0.830}Si_{0.116}Sn_{0.053}$, and [F] $Ge_{0.775}Si_{0.161}Sn_{0.064}$. Insets in E show the high-resolution TEM image of an individual $Ge_{0.830}Si_{0.116}Sn_{0.053}$ QD showing lattice fringes. Average QD diameters and synthetic details are shown in Supporting Information, Table S4.

therefore, the Sn−Ge vibration is observed at a lower frequency. This causes GeSiSn alloys to show broad asymmetric peaks at ∼280−290 cm^{-1}, depending on the composition, with higher Sn compositions showing more pronounced redshifts from the pure Ge peak at 300 cm^{-1}. The effect of Si on Raman shift is much weaker than that of Sn because of compatible lattice parameters of Si and Ge (5.431 Å vs 5.646 Å). The other important factor is the diameter of NCs. Even for phase pure Ge and Si NCs, as the particle size decreases, Raman peaks red-shift, and become broader. This effect is attributed to the phonon confinement model and has been extensively reviewed in the literature.[47,48] It can also be seen that the intensity of the Ge−Si peak is the lowest for $Ge_{0.921}Si_{0.033}Sn_{0.046}$ NCs and increases proportionally with increasing Si. Taken together, the red-shifting of the Ge−Ge vibration and the appearance of a new Ge−Si peak in ternary alloy NCs support the successful alloying of Si and Sn with diamond cubic Ge.

Solid-state reflectance spectra of larger alloy NCs were recorded and converted to absorption to investigate the effects of alloying on optical properties (Supporting Information, Figure S4).[38,39] For ternary alloy NCs, energy gaps depend on both the size and composition. Although the composition was probed accurately, larger alloys were polydisperse and

https://doi.org/10.1021/acs.chemmater.3c01644
Chem. Mater. 2023, 35, 9007−9018

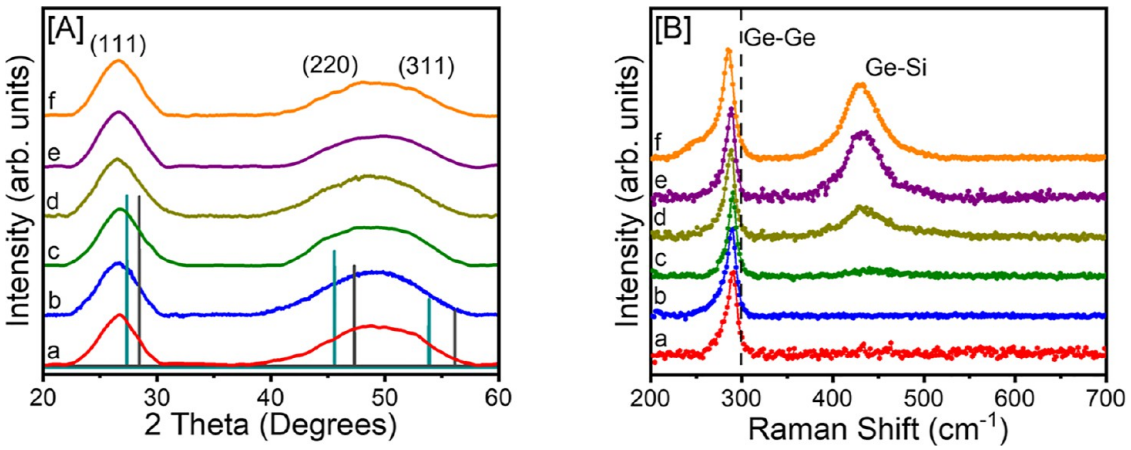

Figure 6. [A] PXRD patterns and [B] Raman spectra of (a) $Ge_{0.935}Si_{0.009}Sn_{0.056}$, (b) $Ge_{0.945}Si_{0.021}Sn_{0.034}$, (c) $Ge_{0.899}Si_{0.033}Sn_{0.068}$, (d) $Ge_{0.907}Si_{0.075}Sn_{0.018}$, (e) $Ge_{0.830}Si_{0.116}Sn_{0.053}$, and (f) $Ge_{0.775}Si_{0.161}Sn_{0.064}$ alloy QDs. Reference patterns shown in [A] are diamond cubic Ge (cyan, JCPDS no. 01-89-5011) and Si (gray, JCPDS # 01-085-8586). The dash line in [B] represents the bulk Ge−Ge vibration at 300 cm^{-1}.

therefore, it was difficult to accurately estimate the absorption onsets. A qualitative analysis of absorption spectra reveals a consistent increase in absorption over the 2.0−3.0 eV energy range, in comparison to 1.0−2.0 eV, for all compositions studied. This suggests a blueshift in the energy gaps relative to the literature value of bulk Ge (0.66 eV) caused by Si incorporation. It can also be seen that the samples with a higher Sn content show a pronounced increase in absorption, in comparison to the lowest Sn containing sample (i.e., $Ge_{0.921}Si_{0.033}Sn_{0.046}$). This effect has been identified in prior studies of group IV alloys that show higher Sn contents and is attributed to increased oscillator strengths of optical transitions caused by higher lattice disorder, which enhances the absorption efficiency of group IV alloys.[14,31,49,50]

Synthesis of Quantum-Confined $Ge_{1-x-y}Si_ySn_x$ Alloy NCs. To elucidate the effects of both Si/Sn alloying and quantum confinement on optical properties, a set of significantly smaller QDs were produced. This has been accomplished by manipulating the growth phase of alloys and limiting it to 5 min at 300 °C. It was also found that a greater percentage of Si incorporation is easier to reach with the synthesis of smaller alloys. This is likely because shorter growth times limit the occurrence of solid-state diffusion, where the competition between Si and Sn may cause Si to dominate. Smaller particles show a quasi-spherical morphology and improved colloidal stability while also facilitating higher Si content, which allows for thorough investigation into optical properties and confinement effects over a wide range of Si and Sn compositions.

To identify particle morphology and verify colloidal stability, representative bright-field TEM images of QDs are recorded and are shown in Figure 5A−F. All compositions show a quasi-spherical morphology and narrow size dispersity without hard edges or polygonal particles. The average particle size varies in the range of 3.2 ± 0.6−4.2 ± 1.1 nm for all QDs. Although Sn compositions were kept within a narrow range (1.8−6.4%), we attained a wider range of Si compositions (0.9−16.1%) for a thorough investigation of the influence of Si on optical properties. As the Si content increases, the contrast between QDs and carbon background decreases, due to mass of Si being much closer to carbon than Ge or Sn. It was also found that the $Ge_{1-x-y}Si_ySn_x$ QDs are colloidally stable in nonpolar solvents because of surface passivation by OLA and ODE ligands (Supporting Information, Figure S5).[51] It is also possible that there are some residual butyl groups on the surface from *n*-BuLi used during the synthesis, which can further contribute to nonpolar surface passivation. The shorter growth times (5 min) are imperative for synthesis of quantum confined alloys, whereas longer (15 min) growth times produced larger polygonal NCs (Figure 4). The size dispersity is improved through size-selective precipitation, allowing the isolation of narrowly dispersed QD sizes for systematic investigation of optical properties.

X-ray diffraction patterns of the smaller $Ge_{1-x-y}Si_ySn_x$ alloy QDs are displayed in Figure 6A. Because these particles are ultrasmall, significant Scherrer broadening has caused the (220) and (311) peaks to blend together, similar to prior studies on smaller Ge and GeSn alloy NCs.[12,14,28,31] The average crystallite sizes were calculated manually by applying the Scherrer equation[52] to the prominent (111) reflection (Supporting Information, Table S2), which were found in the range of ∼1.9−2.3 nm. The largest crystallite diameter corresponds to the composition with the highest Sn/Si ratio, reaffirming the notion of Sn-promoted crystallinity. It can also be seen that the principle (111) peak has shifted to lower 2θ angles relative to the diamond cubic Ge reference pattern because of the lattice expansion induced by Sn, similar to that observed for larger NCs (Figure 4A). The principle peak position remains within the range of 2θ = 26.54−26.77°, indicating that Si has a negligible influence on the (111) peak position, due to compatible lattice parameters of Si and Ge. Overall, Sn promotes the crystallinity and crystallite size of alloy NCs and QDs, whereas Si greatly influences the energy gaps and optical properties.

Phonon modes for the smaller $Ge_{1-x-y}Si_ySn_x$ QDs were evaluated via Raman spectroscopy (Figure 6B). Here, the peaks corresponding to the Ge−Ge vibration span a range of 285.0−291.4 cm^{-1} (Supporting Information, Table S4). This constitutes a red shift from bulk Ge at 300 cm^{-1} and single-element Ge NCs, which span a range of 288−293 cm^{-1} depending on the particle diameter. The shift to a lower frequency is attributed to the combined effects of alloying and phonon confinement, similar to Figure 4B. However, it is likely that the redshifts observed in QDs are more attributable to size effects, whereas those of the larger NCs are mostly caused by the alloying induced lattice disorder. This can be visualized in

https://doi.org/10.1021/acs.chemmater.3c01644
Chem. Mater. 2023, 35, 9007−9018

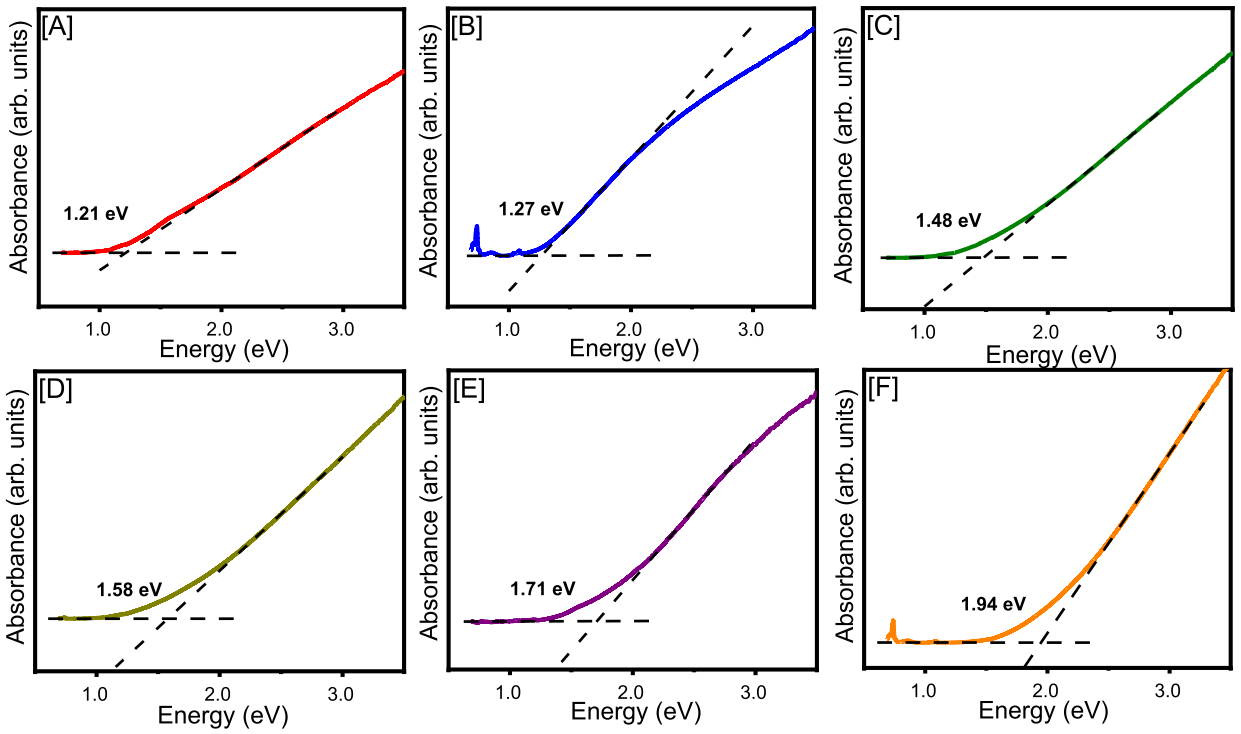

Figure 7. Solid-state absorption spectra converted from reflectance data through use of the Kubelka–Munk method.[38,39] Absorption onsets were traced via a least-squares linear regression, with R^2 values listed in Supporting Information, Table S4. Corresponding energy gaps are printed for each composition: (A) $Ge_{0.935}Si_{0.009}Sn_{0.056}$, (B) $Ge_{0.945}Si_{0.021}Sn_{0.034}$, (C) $Ge_{0.899}Si_{0.033}Sn_{0.068}$, (D) $Ge_{0.907}Si_{0.075}Sn_{0.018}$, (E) $Ge_{0.830}Si_{0.116}Sn_{0.053}$, and (F) $Ge_{0.775}Si_{0.161}Sn_{0.064}$ alloy QDs.

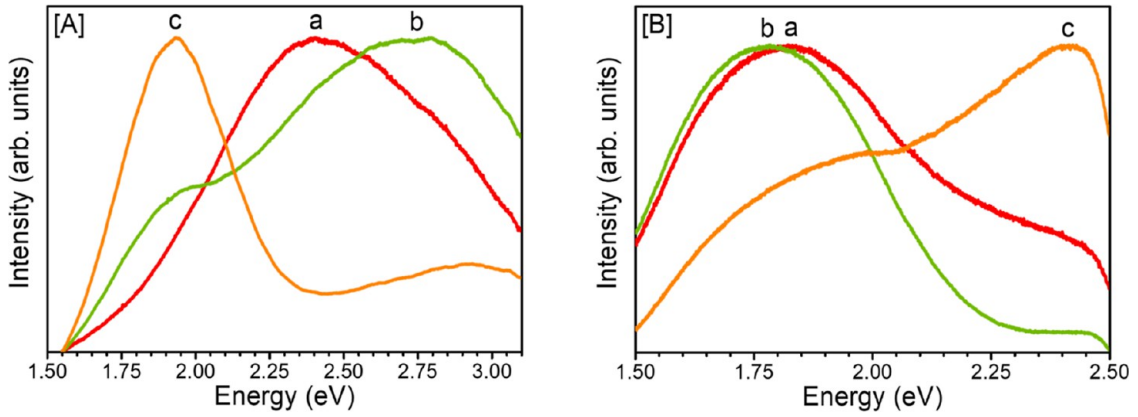

Figure 8. Representative normalized PL spectra obtained for (a) $Ge_{0.935}Si_{0.009}Sn_{0.056}$, (b) $Ge_{0.907}Si_{0.075}Sn_{0.018}$, and (c) $Ge_{0.775}Si_{0.161}Sn_{0.064}$ QDs under (A) 325 nm excitation (~12 W/cm^2) in ambient air and (B) 405 nm excitation (~195 W/cm^2) in a vacuum environment (spectra filtered above ~2.5 eV).

the Ge–Ge peak of $Ge_{0.775}Si_{0.161}Sn_{0.064}$ QDs (Figure 6B), which is more asymmetric than the other peaks and shows a broad shoulder to the left. This is characteristic for Ge-based nanostructures, which are experiencing significant degree of phonon confinement effects. Because $Ge_{0.775}Si_{0.161}Sn_{0.064}$ QDs exhibit the smallest diameter (3.2 ± 0.6 nm), these particles experience stronger confinement effects than other QDs. While compositions a–c [corresponding to $Ge_{0.935}Si_{0.009}Sn_{0.056}$ (a), $Ge_{0.945}Si_{0.021}Sn_{0.034}$ (b), and $Ge_{0.899}Si_{0.033}Sn_{0.068}$ (c), respectively] display a single Raman peak characteristic of the Ge–Ge vibration, a peak corresponding to the Ge–Si vibration appears for alloy QDs containing ≥7.5% Si, which becomes more pronounced for $Ge_{0.830}Si_{0.116}Sn_{0.053}$ and $Ge_{0.775}Si_{0.161}Sn_{0.064}$ QDs. Studies on bulk and thin-film GeSi alloys suggest that the position and the intensity of Ge–Si phonon mode are directly proportional to the Si composition. The high intensity of Ge–Si vibration observed for high Si containing alloys further demonstrates the successful alloying of Si with the diamond cubic Ge.

Solid-state absorption spectra of $Ge_{1-x-y}Si_ySn_x$ QDs (Figures 7 and Supporting Information, S6) were obtained from diffuse reflectance spectra using the Kubelka–Munk remission function. Smaller alloy QDs (~3.2–4.2 nm) show well-defined and more pronounced absorption onsets in comparison to larger (~10–25 nm) alloy NCs. This is because the small QDs are narrowly disperse, consisting of particles having similar diameters, where Si and Sn compositions are expected to dominate the optical properties. The absorption onsets of QDs

https://doi.org/10.1021/acs.chemmater.3c01644
Chem. Mater. 2023, 35, 9007–9018

were probed by applying the least-squares linear regression analysis.[53] The intersection between the onset and the baseline was estimated as the lowest energy at which photons can be effectively absorbed by the material, i.e., the energy gap. The absorption onsets estimated for $Ge_{1-x-y}Si_ySn_x$ alloy QDs range from 1.21−1.94 eV for x = 1.8−6.4% and y = 0.9−16.1% compositions, which are significantly blue-shifted from those of $Si_{0.04}Ge_{0.96-y}Sn_y$ alloy thin films (band gap = 0.7−0.6 eV for y = 8.3−5.1%),[22] which is consistent with the effects of quantum confinement. Moreover, a systematic increase in absorption onsets with increasing Si content was observed for QDs with a relatively narrow range of Sn (1.8−6.4%) composition. These gaps are notably wider than those reported for 3.4−4.6 nm GeSn alloy QDs, which featured energy gaps of 0.75−1.29 eV for 0−11% Sn compositions.

PL spectra recorded from selected $Ge_{1-x-y}Si_ySn_x$ QDs drop-cast on Si substrates are displayed in Figure 8A. These spectra were obtained via short-duration (<2 min, to avoid potential latent surface damage) 325 nm excitation in an ambient atmosphere. For relatively high Si-containing samples, $Ge_{0.907}Si_{0.075}Sn_{0.018}$ and $Ge_{0.775}Si_{0.161}Sn_{0.064}$ QDs, prominent PL peaks were observed in the low-energy region, appearing at 1.98 and 1.93 eV, respectively. These peak energies are in close agreement with the corresponding solid-state absorption onsets (Figure 7), thus suggesting recombination channels within the quantum-confined cores of the alloys as their origin.[54] The additional relatively broad high energy peaks present in all samples fall within a range of 2.42−2.92 eV, blue-shifting correspondingly with increasing Si content. The significant blue shifts ($\gtrsim$ 1 eV) observed from corresponding absorption onsets, however, suggest that these peaks are unlikely to result from transitions within the confined QD core, but are instead related to surface states.[55] The strong positional dependence associated with these peaks can be attributed to variations across the drop-cast sample area.

In order to rule out potential confounding factors contributing to PL, such as photoinduced oxidation or surface modification,[54,56] subsequent measurements were performed under vacuum (Supporting Information, Figure S7) and with lower energy 405 nm (3.06 eV) excitation. The lower energy excitation also served to suppress the high-energy emission (2.42−2.92 eV) and made the low-energy emission more prominent. As shown in Figure 8B, illumination at 405 nm revealed the low-energy emission more clearly (along with reduction in excitation/emission of the aforementioned high energy states) in all three samples, with peaks ranging from 1.77−1.97 eV. While such tunability may in part have its origins in slight variation of the QD diameter, much higher PL energies compared to those from the previously reported $Ge_{1-x}Sn_x$ QDs suggest strong compositional tunability via Si incorporation within the ternary alloy QDs.[12]

To compare the absorption and PL properties of alloy QDs with computational energy gaps, phase pure Ge and Si QDs with ∼2.1 nm diameter were generated and optimized at the SPW92/def2-SVP level of theory, which produced 5.6469 and 5.4393 lattice constants, respectively, in agreement with the experimental lattice constants of 5.6575 and 5.4310 with ∼0.19 and ∼0.15% errors, respectively. The HLE16/CRENBL-computed gaps for the optimized ∼2.1 nm Ge and Si QDs were 2.512 and 3.094 eV, respectively, in agreement with literature reports.[57,58] The extrapolation scheme with bias correction asymptotically reproduced the bulk band gap of Ge,[59] using gap energies calculated for 1.401, 1.715, 2.131, 2.478, and 2.783 nm Ge QDs, where the bias correction accurately predicted the bulk band gap (0.672 eV) at 12 nm (Figure S8). Beyond this point, overextrapolation results in an underestimated energy gap for bulk Ge; thus, the accuracy of extrapolation scheme declines at larger sizes (>12 nm). The theoretical energies obtained for 12 nm (considered bulk) $Ge_{0.95-y}Si_ySn_{0.05}$ alloys using the above approach are 0.721, 0.771, 0.776, and 0.903 eV for y = 5, 10, 15, and 20%, respectively. Although the as-synthesized $Ge_{1-x-y}Si_ySn_x$ QDs slightly differ in composition, the predicted energy gaps obtained from the extrapolation scheme generally agree with their experimental energy gaps (Figure 9). For instance,

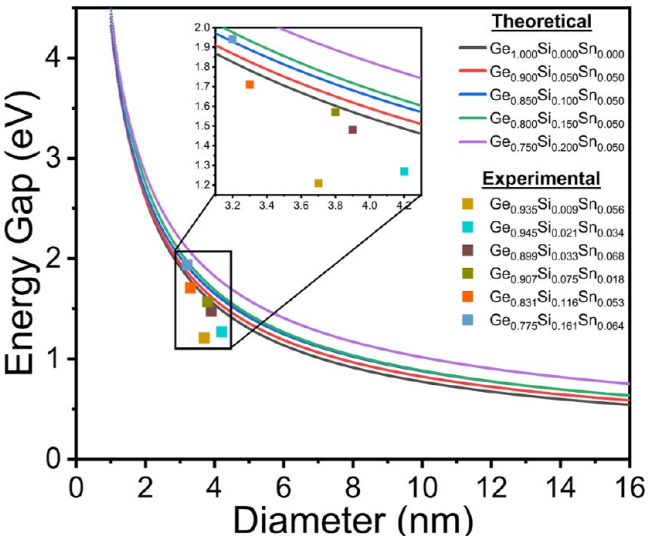

Figure 9. Extrapolated energy gaps of diamond cubic Ge and $Ge_{1-x-y}Si_ySn_x$ alloy QDs obtained via the bias correction scheme along with experimental energy gaps of alloy QDs. The colored lines are computational energy gaps, and the colored symbols are experimental energy gaps.

$Ge_{0.831}Si_{0.116}Sn_{0.053}$ QDs with 3.3 ± 0.3 nm diameter show an experimental gap of 1.71 eV, whereas the predicted gap for $Ge_{0.85}Si_{0.10}Sn_{0.05}$ is ∼1.86 eV (Figure 9). Likewise, $Ge_{0.775}Si_{0.161}Sn_{0.064}$ QDs with 3.2 ± 0.3 nm diameter show an experimental energy gap of 1.94 eV, while the computational gap for $Ge_{0.80}Si_{0.15}Sn_{0.05}$ is ∼1.95 eV. Increased Si content in the alloy increases the energy gaps, and this trend is respected throughout the extrapolation curves. As the particle size decreases, the computed energy gap increases exponentially, in accordance with quantum confinement, although the trends observed for Si and Sn compositions remain consistent. This behavior constitutes an expansion in the library of energy gaps achievable for group IV materials and their alloys as well as the preservation of composition-based tunability, a unique property that distinguishes group IV alloys from other semiconductor nanostructures.

CONCLUSIONS

We have developed a facile colloidal route for the synthesis of quantum-confined and nonquantum-confined $Ge_{1-x-y}Si_ySn_x$ alloys that show variable Si (0.9−16.1%) and Sn (1.8−14.9%) compositions and diameters in the range of ∼3−25 nm. The synthesis involved coreduction of halide precursors, followed by the growth of ternary alloy seeds at 300 °C for different times to produce homogeneous alloys. Electron

https://doi.org/10.1021/acs.chemmater.3c01644
Chem. Mater. 2023, 35, 9007−9018

microscopy studies reveal that the larger NCs are quasi-spherical at lower Sn compositions and grow into polygonal crystallites with increasing Sn composition. HAADF images and STEM-EDS elemental maps affirm the structural homogeneity of all samples. PXRD data confirm the perseverance of diamond cubic Ge structure and a shift of diffraction patterns to lower 2θ angles owing to lattice expansion from Sn incorporation. Raman spectra show a red shift of the Ge−Ge phonon mode because of combined effects of Sn alloying and quantum confinement and emergence of a Ge−Si peak, which is consistent with the synthesis of homogeneous ternary alloys. The electronic structure probed via solid-state absorption spectroscopy indicate strong composition-tunable absorption onsets in the visible to near IR spectrum (1.21−1.94 eV), for QDs with 0.9−16.1 and 1.8−6.8% Si and Sn compositions, respectively. Consistent with absorption spectra, the emission spectra of alloy QDs show low-energy (1.77−1.97 eV) and high-energy (2.42−2.92 eV) PL peaks, which we attribute to radiative recombination from core and surface states, respectively. The absorption onsets estimated for $Ge_{1-y-x}Si_ySn_x$ QD range from 1.21−1.94 eV for x = 1.8−6.4% and y = 0.9−16.1% compositions, which are significantly blue-shifted from those reported for $Si_{0.04}Ge_{0.96-y}Sn_y$ bulk alloy films (band gap = 0.7−0.6 eV for y = 8.3−5.1%).[22,58] This constitutes a noteworthy expansion in the optical properties that can be achievable for group IV alloy NCs and QDs. Although absorption and PL properties were probed using drop-cast solid-state samples, congruent with future thin-film device applications, extensive solution-state characterization of $Ge_{1-x-y}Si_ySn_x$ alloy QDs including PL quantum yield measurements, and the synthesis of different size range (2−10 nm) nanoalloys with control over structure and composition are currently underway. These studies will be reported elsewhere.

■ ASSOCIATED CONTENT

Supporting Information

The Supporting Information is available free of charge at https://pubs.acs.org/doi/10.1021/acs.chemmater.3c01644.

Experimental parameters used in the synthesis of bulk-like and quantum-confined $Ge_{1-x-y}Si_ySn_x$ alloys, nominal and empirical compositions, particle and crystallite sizes, Raman peak positions, lattice parameters, and absorption energy onsets; additional STEM images, STEM-HAADF elemental maps, EDS spectra, absorption and FT-IR spectra of larger $Ge_{1-x-y}Si_ySn_x$ alloy NCs; solid-state absorption spectra of smaller $Ge_{1-x-y}Si_ySn_x$ alloy QDs; representative normalized PL spectra obtained for selected QDs under vacuum; and determination of the optimal number of points needed for the energy-gap extrapolation scheme with the bias correction (PDF)

■ AUTHOR INFORMATION

Corresponding Author

Indika U. Arachchige − *Department of Chemistry, Virginia Commonwealth University, Richmond, Virginia 23284-2006, United States;* orcid.org/0000-0001-6025-5011; Email: iuarachchige@vcu.edu

Authors

Drew Spera − *Department of Chemistry, Virginia Commonwealth University, Richmond, Virginia 23284-2006, United States*

David Pate − *Department of Electrical and Computer Engineering, Virginia Commonwealth University, Richmond, Virginia 23284-3068, United States;* orcid.org/0000-0002-1497-651X

Griffin C. Spence − *Department of Chemistry, Virginia Commonwealth University, Richmond, Virginia 23284-2006, United States*

Corentin Villot − *Department of Chemistry, Virginia Commonwealth University, Richmond, Virginia 23284-2006, United States*

Chineme Jeanfrances Onukwughara − *Department of Chemistry, Virginia Commonwealth University, Richmond, Virginia 23284-2006, United States*

Daulton White − *Department of Chemistry, Virginia Commonwealth University, Richmond, Virginia 23284-2006, United States*

Ka Un Lao − *Department of Chemistry, Virginia Commonwealth University, Richmond, Virginia 23284-2006, United States;* orcid.org/0000-0002-3993-536X

Ümit Özgür − *Department of Electrical and Computer Engineering, Virginia Commonwealth University, Richmond, Virginia 23284-3068, United States*

Complete contact information is available at: https://pubs.acs.org/10.1021/acs.chemmater.3c01644

Author Contributions

D.S. contributed to the NC synthesis and preliminary drafting of the manuscript. D.P. and U.O. probed the PL properties. G.S. and I.A. completely revised the manuscript. C.J.O. and D.W. contributed to synthesis of a few alloy compositions. C.V. and K.U.L. probed the theoretical energy gaps. All authors have given approval to the final version of the manuscript.

Notes

The authors declare no competing financial interest.

■ ACKNOWLEDGMENTS

The authors gratefully acknowledge the financial support by the US National Science Foundation DMR-2211606 award and the Department of Chemistry and Department of Electrical and Computer Engineering at Virginia Commonwealth University.

■ REFERENCES

(1) Sun, Z.; Chen, X.; He, Y.; Li, J.; Wang, J.; Yan, H.; Zhang, Y. Toward Efficiency Limits of Crystalline Silicon Solar Cells: Recent Progress in High-Efficiency Silicon Heterojunction Solar Cells. *Adv. Energy Mater.* **2022**, *12*, 2200015.

(2) Liyanage, D.; Spera, D. Z.; Sarkar, R.; Troesch, B. P.; Nakagawara, T. A.; Ozgur, U.; Arachchige, I. U. CdSe/Ag Hybrid Aerogels: Integration of Plasmonic and Excitonic Properties of Metal-Semiconductor Nanostructures via Sol-Gel Assembly. *Adv. Photonics Res.* **2022**, *3*, 2200026.

(3) Ke, J. Semiconductor Nanocrystals for Environmental Catalysis. In *Advanced Nanomaterials for Pollutant Sensing and Environmental Catalysis*; Zhao, Q., Ed.; Elsevier, 2020; Chapter 4, pp 119−163.

(4) Khalafallah, D.; Sarkar, R.; Demir, M.; Khalil, K. A.; Hong, Z.; Farghaly, A. A. Heteroatoms-Doped Carbon Nanotubes for Energy Applications. In *Handbook of Carbon Nanotubes*; Abraham, J., Thomas, S., Kalarikkal, N., Eds.; Springer International Publishing: Cham, 2020; pp 1−39.

(5) Eladgham, E. H.; Rodene, D. D.; Sarkar, R.; Arachchige, I. U.; Gupta, R. B. Electrocatalytic Activity of Bimetallic Ni-Mo-P Nanocrystals for Hydrogen Evolution Reaction. *ACS Appl. Nano Mater.* **2020**, *3*, 8199−8207.
(6) Tran, H.; Pham, T.; Margetis, J.; Zhou, Y.; Dou, W.; Grant, P. C.; Grant, J. M.; Al-Kabi, S.; Sun, G.; Soref, R. A.; Tolle, J.; Zhang, Y.-H.; Du, W.; Li, B.; Mortazavi, M.; Yu, S.-Q. Si-Based GeSn Photodetectors toward Mid-Infrared Imaging Applications. *ACS Photonics* **2019**, *6*, 2807−2815.
(7) Martynenko, I. V.; Litvin, A. P.; Purcell-Milton, F.; Baranov, A. V.; Fedorov, A. V.; Gun'ko, Y. K. Application of Semiconductor Quantum Dots in Bioimaging and Biosensing. *J. Mater. Chem. B* **2017**, *5*, 6701−6727.
(8) Algar, W. R. Heroes or Villains? How Nontraditional Luminescent Materials Do and Do Not Enhance Bioanalysis and Imaging. *Chem. Mater.* **2020**, *32*, 4863−4883.
(9) Sharma, M.; Tripathi, S. K. Analysis of Interface States and Series Resistance for Al/PVA:N-CdS Nanocomposite Metal-Semiconductor and Metal-Insulator-Semiconductor Diode Structures. *Appl. Phys. A: Mater. Sci. Process.* **2013**, *113*, 491−499.
(10) Tanusilp, S.; Kurosaki, K. Rare-Earth Silicides: The Promising Candidates for Thermoelectric Applications at near Room Temperature. *Jpn. J. Appl. Phys.* **2023**, *62*, SD0802.
(11) Amatya, R.; Ram, R. J. Trend for Thermoelectric Materials and Their Earth Abundance. *J. Electron. Mater.* **2012**, *41*, 1011−1019.
(12) Esteves, R. J. A.; Ho, M. Q.; Arachchige, I. U. Nanocrystalline Group IV Alloy Semiconductors: Synthesis and Characterization of $Ge_{1-x}Sn_x$ Quantum Dots for Tunable Bandgaps. *Chem. Mater.* **2015**, *27*, 1559−1568.
(13) Hafiz, S. A.; Esteves, R. J. A.; Demchenko, D. O.; Arachchige, I. U.; Özgür, Ü. Energy Gap Tuning and Carrier Dynamics in Colloidal $Ge_{1-x}Sn_x$ Quantum Dots. *J. Phys. Chem. Lett.* **2016**, *7*, 3295−3301.
(14) Alan Esteves, R. J.; Hafiz, S.; Demchenko, D. O.; Özgür, Ü.; Arachchige, I. U. Ultra-Small $Ge_{1-x}Sn_x$ Quantum Dots with Visible Photoluminescence. *Chem. Commun.* **2016**, *52*, 11665−11668.
(15) Ryu, M.-Y.; Harris, T. R.; Yeo, Y. K.; Beeler, R. T.; Kouvetakis, J. Temperature-Dependent Photoluminescence of Ge/Si and $Ge_{1-y}Sn_y$/Si, Indicating Possible Indirect-to-Direct Bandgap Transition at Lower Sn Content. *Appl. Phys. Lett.* **2013**, *102*, 171908.
(16) Ribas, M. A.; Singh, A. K.; Sorokin, P. B.; Yakobson, B. I. Patterning Nanoroads and Quantum Dots on Fluorinated Graphene. *Nano Res.* **2011**, *4*, 143−152.
(17) Mathews, J.; Beeler, R. T.; Tolle, J.; Xu, C.; Roucka, R.; Kouvetakis, J.; Menéndez, J. Direct-Gap Photoluminescence with Tunable Emission Wavelength in $Ge_{1-y}Sn_y$ Alloys on Silicon. *Appl. Phys. Lett.* **2010**, *97*, 221912.
(18) Gupta, S.; Magyari-Köpe, B.; Nishi, Y.; Saraswat, K. C. Achieving Direct Band Gap in Germanium through Integration of Sn Alloying and External Strain. *J. Appl. Phys.* **2013**, *113*, 073707.
(19) Zhang, D.; Jin, L.; Li, J.; Wen, T.; Liu, C.; Xu, F.; Kolodzey, J.; Liao, Y. MBE Growth of Ultra-Thin GeSn Film with High Sn Content and Its Infrared/Terahertz Properties. *J. Alloys Compd.* **2016**, *665*, 131−136.
(20) Gencarelli, F.; Vincent, B.; Souriau, L.; Richard, O.; Vandervorst, W.; Loo, R.; Caymax, M.; Heyns, M. Low-Temperature Ge and GeSn Chemical Vapor Deposition Using Ge_2H_6. *Thin Solid Films* **2012**, *520*, 3211−3215.
(21) Timofeev, V.; Nikiforov, A.; Yakimov, A.; Mashanov, V.; Loshkarev, I.; Bloshkin, A.; Kirienko, V.; Novikov, V.; Kareva, K. Studying the Morphology, Structure and Band Diagram of Thin GeSiSn Films and Their Mid-Infrared Photoresponse. *Semicond. Sci. Technol.* **2019**, *34*, 014001.
(22) Wirths, S.; Buca, D.; Mantl, S. Si-Ge-Sn Alloys: From Growth to Applications. *Prog. Cryst. Growth Charact. Mater.* **2016**, *62*, 1−39.
(23) Xu, C.; Jiang, L.; Kouvetakis, J.; Menéndez, J. Optical Properties of $Ge_{1-x-y}Si_xSn_y$ Alloys with y > x: Direct Bandgaps beyond 1550 Nm. *Appl. Phys. Lett.* **2013**, *103*, 072111.
(24) Gallagher, J. D.; Xu, C.; Jiang, L.; Kouvetakis, J.; Menéndez, J. Fundamental Band Gap and Direct-Indirect Crossover in $Ge_{1-x-y}Si_xSn_y$ Alloys. *Appl. Phys. Lett.* **2013**, *103*, 202104.
(25) Xie, J.; Chizmeshya, A. V. G.; Tolle, J.; D'Costa, V. R.; Menendez, J.; Kouvetakis, J. Synthesis, Stability Range, and Fundamental Properties of Si-Ge-Sn Semiconductors Grown Directly on Si(100) and Ge(100) Platforms. *Chem. Mater.* **2010**, *22*, 3779−3789.
(26) Nakamura, M.; Shimura, Y.; Takeuchi, S.; Nakatsuka, O.; Zaima, S. Growth of $Ge_{1-x}Sn_x$ Heteroepitaxial Layers with Very High Sn Contents on InP(001) Substrates. *Thin Solid Films* **2012**, *520*, 3201−3205.
(27) Arimoto, K.; Watanabe, M.; Yamanaka, J.; Nakagawa, K.; Sawano, K.; Shiraki, Y.; Usami, N.; Nakajima, K. Growth Temperature Dependence of the Crystalline Morphology of SiGe Films Grown on Si(110) Substrates with Compositionally Step-Graded Buffer. *Thin Solid Films* **2008**, *517*, 235−238.
(28) Ramasamy, K.; Kotula, P. G.; Modine, N.; Brumbach, M. T.; Pietryga, J. M.; Ivanov, S. A. Cubic SnGe Nanoalloys: Beyond Thermodynamic Composition Limit. *Chem. Commun.* **2019**, *55*, 2773−2776.
(29) Ramasamy, K.; Kotula, P. G.; Fidler, A. F.; Brumbach, M. T.; Pietryga, J. M.; Ivanov, S. A. Sn_xGe_{1-x} Alloy Nanocrystals: A First Step toward Solution-Processed Group IV Photovoltaics. *Chem. Mater.* **2015**, *27*, 4640−4649.
(30) Demchenko, D. O.; Tallapally, V.; Esteves, R. J. A.; Hafiz, S.; Nakagawara, T. A.; Arachchige, I. U.; Özgür, Ü. Optical Transitions and Excitonic Properties of $Ge_{1-x}Sn_x$ Alloy Quantum Dots. *J. Phys. Chem. C* **2017**, *121*, 18299−18306.
(31) Tallapally, V.; Nakagawara, T. A.; Demchenko, D. O.; Özgür, Ü.; Arachchige, I. U. $Ge_{1-x}Sn_x$ Alloy Quantum Dots with Composition-Tunable Energy Gaps and near-Infrared Photoluminescence. *Nanoscale* **2018**, *10*, 20296−20305.
(32) Barbieri, R. C.; Ding, K.; Özgür, Ü.; Arachchige, I. U. Solution-Processed $Ge_{1-x}Sn_x$ Alloy Nanocrystal Thin Films with High Electrical Conductivity and Tunable Energy Gaps. *Chem. Mater.* **2021**, *33*, 6897−6908.
(33) Fischer, I. A.; Wendav, T.; Augel, L.; Jitpakdeebodin, S.; Oliveira, F.; Benedetti, A.; Stefanov, S.; Chiussi, S.; Capellini, G.; Busch, K.; Schulze, J. Growth and Characterization of SiGeSn Quantum Well Photodiodes. *Opt. Express* **2015**, *23*, 25048−25057.
(34) Moontragoon, P.; Pengpit, P.; Burinprakhon, T.; Maensiri, S.; Vukmirovic, N.; Ikonic, Z.; Harrison, P. Electronic Properties Calculation of $Ge_{1-x-y}Si_xSn_y$ Ternary Alloy and Nanostructure. *J. Non-Cryst. Solids* **2012**, *358*, 2096−2098.
(35) Spera, D. Z.; Arachchige, I. U. Improved Surface Passivation of Colloidal $Ge_{1-x}Sn_x$ Nanoalloys through Amorphous SiO_2 Shell Growth. *J. Phys. Chem. C* **2022**, *126*, 9862−9874.
(36) Kowalczyk, B.; Lagzi, I.; Grzybowski, B. A. Nanoseparations: Strategies for Size and/or Shape-Selective Purification of Nanoparticles. *Curr. Opin. Colloid Interface Sci.* **2011**, *16*, 135−148.
(37) Gravelsins, S.; Dhirani, A.-A. A Rapid, High Yield Size-Selective Precipitation Method for Generating Au Nanoparticles in Organic Solvents with Tunably Monodisperse Size Distributions and Replaceable Ligands. *RSC Adv.* **2017**, *7*, 55830−55834.
(38) Tsuge, A.; Uwamino, Y.; Ishizuka, T.; Suzuki, K. Quantitative Analysis of Powdery Sample by Diffuse Reflectance Infrared Fourier Transform Spectrometry: Determination of the α-Component in Silicon Nitride. *Appl. Spectrosc.* **1991**, *45*, 1377−1380.
(39) Nowak, M.; Kauch, B.; Szperlich, P. Determination of Energy Band Gap of Nanocrystalline SbSI Using Diffuse Reflectance Spectroscopy. *Rev. Sci. Instrum.* **2009**, *80*, 046107.
(40) Epifanovsky, E.; Gilbert, A. T. B.; Feng, X.; Lee, J.; Mao, Y.; Mardirossian, N.; Pokhilko, P.; White, A. F.; Coons, M. P.; Dempwolff, A. L.; et al. Software for the Frontiers of Quantum Chemistry: An Overview of Developments in the Q-Chem 5 Package. *J. Chem. Phys.* **2021**, *155*, 084801.
(41) Ruddy, D. A.; Johnson, J. C.; Smith, E. R.; Neale, N. R. Size and Bandgap Control in the Solution-Phase Synthesis of Near-Infrared-

https://doi.org/10.1021/acs.chemmater.3c01644
Chem. Mater. 2023, 35, 9007−9018

Emitting Germanium Nanocrystals. *ACS Nano* **2010**, *4* (12), 7459−7466.
(42) Kasper, E.; Werner, J.; Oehme, M.; Escoubas, S.; Burle, N.; Schulze, J. Growth of Silicon Based Germanium Tin Alloys. *Thin Solid Films* **2012**, *520*, 3195−3200.
(43) Adachi, S. Properties of Semiconductor Alloys Group-IV, III-V and II-VI Semiconductors. Wiley series in materials for electronic & optoelectronic applications; Wiley: Chichester, West Sussex, U.K., 2009.
(44) Denton, A. R.; Ashcroft, N. W. Vegard's Law. *Phys. Rev. A* **1991**, *43*, 3161−3164.
(45) Zaima, S.; Nakatsuka, O.; Taoka, N.; Kurosawa, M.; Takeuchi, W.; Sakashita, M. Growth and Applications of GeSn-Related Group-IV Semiconductor Materials. *Sci. Technol. Adv. Mater.* **2015**, *16*, 043502.
(46) Tabatabaei, K.; Holmes, A. L.; Newton, K. A.; Muthuswamy, E.; Sfadia, R.; Carter, S. A.; Kauzlarich, S. M. Halogen-Induced Crystallinity and Size Tuning of Microwave Synthesized Germanium Nanocrystals. *Chem. Mater.* **2019**, *31*, 7510−7521.
(47) Osswald, S.; Mochalin, V. N.; Havel, M.; Yushin, G.; Gogotsi, Y. Phonon Confinement Effects in the Raman Spectrum of Nanodiamond. *Phys. Rev. B* **2009**, *80*, 075419.
(48) Volodin, V. A.; Marin, D. V.; Sachkov, V. A.; Gorokhov, E. B.; Rinnert, H.; Vergnat, M. Applying an Improved Phonon Confinement Model to the Analysis of Raman Spectra of Germanium Nanocrystals. *J. Exp. Theor. Phys.* **2014**, *118*, 65−71.
(49) Lee, P. A.; Ramakrishnan, T. V. Disordered Electronic Systems. *Rev. Mod. Phys.* **1985**, *57*, 287−337.
(50) Abrahams, E.; Anderson, P. W.; Licciardello, D. C.; Ramakrishnan, T. V. Scaling Theory of Localization: Absence of Quantum Diffusion in Two Dimensions. *Phys. Rev. Lett.* **1979**, *42*, 673−676.
(51) Ju, Z.; Qi, X.; Sfadia, R.; Wang, M.; Tseng, E.; Panchul, E. C.; Carter, S. A.; Kauzlarich, S. M. Single-Crystalline Germanium Nanocrystals via a Two-Step Microwave-Assisted Colloidal Synthesis from GeI_4. *ACS Mater. Au* **2022**, *2*, 330−342.
(52) Muniz, F. T. L.; Miranda, M. A. R.; Morilla dos Santos, C.; Sasaki, J. M. The Scherrer Equation and the Dynamical Theory of X-Ray Diffraction. *Acta Crystallogr., Sect. A* **2016**, *72*, 385−390.
(53) Stutz, J.; Platt, U. Numerical Analysis and Estimation of the Statistical Error of Differential Optical Absorption Spectroscopy Measurements with Least-Squares Methods. *Appl. Opt.* **1996**, *35*, 6041−6053.
(54) Wolkin, M. V.; Jorne, J.; Fauchet, P. M.; Allan, G.; Delerue, C. Electronic States and Luminescence in Porous Silicon Quantum Dots: The Role of Oxygen. *Phys. Rev. Lett.* **1999**, *82*, 197−200.
(55) Giansante, C.; Infante, I. Surface Traps in Colloidal Quantum Dots: A Combined Experimental and Theoretical Perspective. *J. Phys. Chem. Lett.* **2017**, *8*, 5209−5215.
(56) Dohnalová, K.; Poddubny, A. N.; Prokofiev, A. A.; de Boer, W. D. A. M.; Umesh, C. P.; Paulusse, J. M. J.; Zuilhof, H.; Gregorkiewicz, T. Surface Brightens up Si Quantum Dots: Direct Bandgap-like Size-Tunable Emission. *Light Sci. Appl.* **2013**, *2*, No. e47.
(57) Borlido, P.; Schmidt, J.; Huran, A. W.; Tran, F.; Marques, M. A. L.; Botti, S. Exchange-Correlation Functionals for Band Gaps of Solids: Benchmark, Reparametrization and Machine Learning. *npj Comput. Mater.* **2020**, *6*, 96.
(58) Borlido, P.; Aull, T.; Huran, A. W.; Tran, F.; Marques, M. A. L.; Botti, S. Large-Scale Benchmark of Exchange-Correlation Functionals for the Determination of Electronic Band Gaps of Solids. *J. Chem. Theory Comput.* **2019**, *15*, 5069−5079.
(59) Jiang, L.; Xu, C.; Gallagher, J. D.; Favaro, R.; Aoki, T.; Menéndez, J.; Kouvetakis, J. Development of Light Emitting Group IV Ternary Alloys on Si Platforms for Long Wavelength Optoelectronic Applications. *Chem. Mater.* **2014**, *26*, 2522−2531.

https://doi.org/10.1021/acs.chemmater.3c01644
Chem. Mater. 2023, 35, 9007−9018